



RESEARCH ARTICLE

10.1002/2015GC005932

Evolution of permeability across the transition from brittle failure to cataclastic flow in porous siltstone

Marco M. Scuderi^{1,2}, Hiroko Kitajima³, Brett M. Carpenter⁴, Demian M. Saffer¹, and Chris Marone¹

Key Points:

- Mapping the brittle-ductile transition in porous siltstone
- Deformation style controls the relation between porosity and permeability
- Shear localization causes abrupt decrease in permeability

Correspondence to:

M. M. Scuderi,
marco.scuderi@uniroma1.it

Citation:

Scuderi, M. M., H. Kitajima, B. M. Carpenter, D. M. Saffer, and C. Marone (2015), Evolution of permeability across the transition from brittle failure to cataclastic flow in porous siltstone, *Geochem. Geophys. Geosyst.*, 16, doi:10.1002/2015GC005932.

Received 28 MAY 2015

Accepted 17 AUG 2015

Accepted article online 20 AUG 2015

¹Department of Geosciences, Pennsylvania State University, State College, Pennsylvania, USA, ²Dipartimento di Scienze della Terra, Università degli studi La Sapienza, Rome, Italy, ³Department of Geology and Geophysics, Texas A&M University, College Station, Texas, USA, ⁴Istituto Nazionale di Geofisica e Vulcanologia, Rome, Italy

Abstract Porous sedimentary rocks fail in a variety of modes ranging from localized, brittle deformation to pervasive, cataclastic flow. To improve our understanding of this transition and its affect on fluid flow and permeability, we investigated the mechanical behavior of a siltstone unit within the Marcellus Formation, PA USA, characterized by an initial porosity ranging from 41 to 45%. We explored both hydrostatic loading paths ($\sigma_1 = \sigma_2 = \sigma_3$) and triaxial loading paths ($\sigma_1 > \sigma_2 = \sigma_3$) while maintaining constant effective pressure ($P_e = P_c - P_p$). Samples were deformed with an axial displacement rate of 0.1 $\mu\text{m/s}$ (strain rate of $2 \times 10^{-6} \text{ s}^{-1}$). Changes in pore water volume were monitored (drained conditions) to measure the evolution of porosity. Permeability was measured at several stages of each experiment. Under hydrostatic loading, we find the onset of macroscopic grain crushing (P^*) at 39 MPa. Triaxial loading experiments show a transition from brittle behavior with shear localization and compaction to cataclastic-flow as confining pressure increases. When samples fail by shear localization, permeability decreases abruptly without significant changes in porosity. Conversely, for cataclastic deformation, permeability reduction is associated with significant porosity reduction. Postexperiment observation of brittle samples show localized shear zones characterized by grain comminution. Our data show how zones of shear localization can act as barriers to fluid flow and thus modify the hydrological and mechanical properties of the surrounding rocks. Our results have important implications for deformation behavior and permeability evolution in sedimentary systems, and in particular where the stress field is influenced by injection or pumping.

1. Introduction

In the upper crust, sedimentary rocks can accommodate deformation in a brittle manner, associated with localized fracturing and faulting, or in a ductile manner, characterized by cataclastic flow and distributed deformation. The transition between these deformation styles has important geophysical and hydrological implications. For example, it has been interpreted as the transition from seismic to aseismic behavior of faults [Sibson, 1982], associated with variations in the hydrological properties of the medium due to different micromechanical processes involved during deformation. In this context, understanding the physical processes across the brittle-ductile transition, and their interrelationship with permeability, is important for a wide range of problems/questions, including: (1) deformation and fluid flow in tectonically active environments; (2) evolution of permeability in reservoirs and aquifers in response to pumping and injection, and (3) the response of crustal hydrogeologic systems to shallow earthquakes [e.g., Vrolijk, 1990; Hyndman and Wang, 1995; Hyndman et al., 1993; Zoback, 2012; Ellsworth, 2013; Improta et al., 2015].

Initial porosity and effective stress determine how sediments will respond to deformation, with the deformation style playing an important role in determining permeability evolution. In the brittle regime, dilation is often associated with strain localization along planar structures, such as faults, characterized by different physicochemical properties than the host rocks [Brace, 1978; Byrne et al., 1988; Marone and Scholz, 1988]. Dilatant failure can induce nucleation/propagation of earthquake ruptures and modify regional fluid flow, with faults acting as conduits or barriers for fluids during the seismic cycle [Sibson, 1982; Byerlee, 1993; Magee and Zoback, 1993]. On the other hand, in the ductile field, mechanical compaction can lead to irreversible porosity loss and inelastic deformation by cataclastic flow and creep mechanisms [Karig, 1990; Zhang et al., 1990a, 1990b; Moore and Vrolijk, 1992; Wong et al., 1997; Vajdova et al., 2004a, 2004b; Karner et al., 2005; Brantut et al., 2012]. In the ductile domain, generalized permeability reduction is controlled by

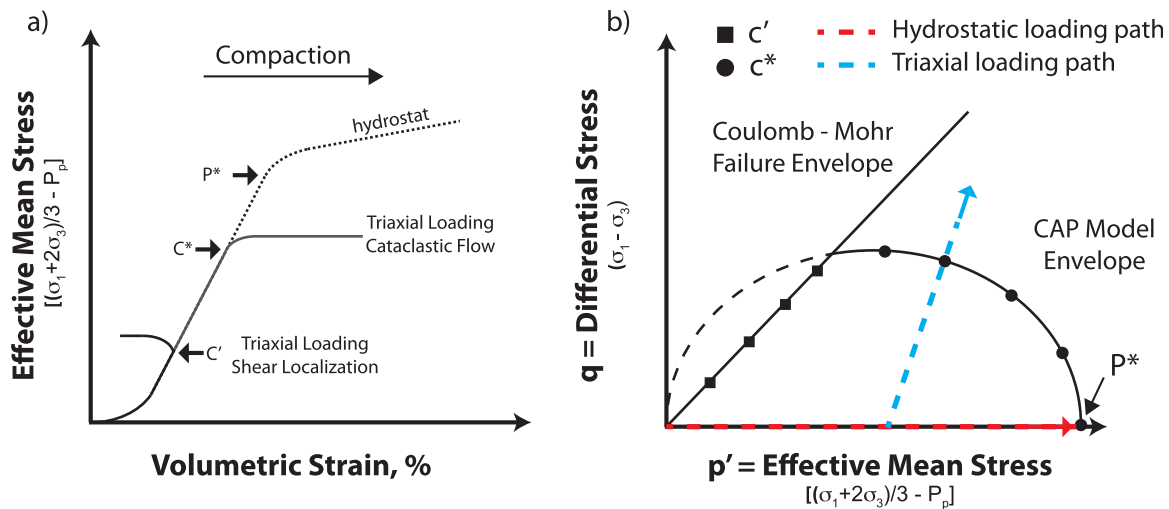


Figure 1. (a) Schematic representation of critical stress states; P^* (onset of grain crushing and pore collapse), C^* (shear-enhanced compaction) and C' (shear-induced dilation) for hydrostatic and triaxial loading paths. (b) Critical stress states reported in a p' - q stress space. The envelope of the critical stresses C' determine a Coulomb-Mohr type failure envelope. The CAP model is determined by the envelope of the critical stresses, C^* .

either homogenous deformation, uniformly distributed within sediments, or heterogeneous, localized deformation with the development of compaction bands or shear deformation bands [Zhu and Wong, 1997; Fossen et al., 2007; Baud et al., 2012; Kaproth et al., 2010].

In this paper, we aim to extend our understanding of the relationship between porosity and permeability during deformation and failure. Our study is based on an exceptionally well-controlled suite of triaxial deformation experiments on siltstones found within the Marcellus Formation, PA, USA, with initial porosities ranging from 40 to 45%. The particular choice of rock type is motivated by: (1) the lack of information about deformation processes in such high porosity rocks; (2) the dearth of detailed data on the mechanical behavior of siltstone; and (3) the importance of this rock type as a hydrocarbon reservoir. Our results show that in the brittle faulting regime, permeability evolution is not well predicted by porosity evolution, which has important implications for hydrologic properties in natural systems undergoing burial or tectonic loading. Shear localization can potentially act as a hydraulic barrier for fluid flow, modifying fluid distribution and potentially generating overpressure, or compartmentalizing fluids.

2. Deformation of Porous Rocks

2.1. Failure Modes and Yield Stresses

The stress field acting on sediments during their burial and deformation history can be reproduced in laboratory experiments by applying a principal compressive stress (σ_1) (i.e., overburden load), which acts vertically, axi-symmetric to the sample, and a confining pressure ($\sigma_3 = \sigma_2$). The axial effective stress is then calculated as the difference between the applied axial stress and pore fluid pressure (σ'_1). Similarly the effective confining pressure (P_e) acting on the sample is calculated as the difference between the confining and pore pressures, $\sigma'_2 = \sigma'_3 = P_e = (P_c - P_p)$ [Hubbert and Rubey, 1959]. For triaxial loading tests, where σ'_1 exceeds $\sigma'_2 = \sigma'_3 = (P_c - P_p)$, the differential stress (σ_d) is calculated as the difference between the axial stress and confining pressure ($\sigma_d = \sigma_1 - P_c$). The overall stress state acting on the sample is described by the effective mean stress as:

$$\sigma'_m = [(\sigma_1 + \sigma_2 + \sigma_3)/3] - P_p \quad (1)$$

We follow standard conventions and refer to the key yield stresses as P^* , C^* and C' [Brace, 1978; Zhang et al., 1990a; Zhang et al., 1990b; David, 1994; Menéndez et al., 1996; Wong et al., 1997] (Figure 1a). With increasing hydrostatic load ($\sigma'_1 = \sigma'_2 = \sigma'_3$), P^* is taken as the point at which compaction starts to accelerate with respect to the linear-elastic behavior and marks the onset of grain crushing and pore collapse, [Brace, 1978; Zhang et al., 1990a; Menéndez et al., 1996]. Under triaxial deformation, samples can fail by shear localization or cataclastic flow [Wong et al., 1997]. C^* indicates the stress state at which the deviatoric stress field

causes an accelerated decrease in porosity (shear-enhanced compaction), relative to that during the hydrostat loading, causing failure through pervasive cataclastic flow [Curran and Carroll, 1979; Menéndez et al., 1996; Wong et al., 1997]. In contrast, C' marks the yield stress at which the deviatoric stress field causes a deceleration of compaction (shear-induced dilation), associated with shear localization and brittle behavior [Menéndez et al., 1996; Wong et al., 1997].

In critical state soil mechanics, the full deformation behavior for soils is usually described in terms of the effective mean stress, $p' = ((\sigma_1 + \sigma_2 + \sigma_3)/3) - P_p$ and the differential stress $q = (\sigma_1 - \sigma_3)/2$. In $q - p'$ space, the yield stresses (C' , C^* and P^*), which are defined by a suite of triaxial deformation experiments, are plotted to construct a failure envelope (Figure 1b). The envelope of yield stresses (C') is commonly fit by a line of the form [Bolton, 1979]:

$$q = C + M'_p \quad (2)$$

where M is related to the angle of internal friction (θ) in the Coulomb failure criteria via the relation [after Bolton, 1979]:

$$\sin(\theta) = 3M / (M + 6) \quad (3)$$

When a sample fails by cataclastic flow, the yield stresses defined by values of C^* are described by an elliptical envelope consistent with the CAP model from soil mechanics [Drucker et al., 1952; Roscoe et al., 1958] of the form [Wong et al., 1997]:

$$[(p'/P^*) - \xi]^2 / (1 - \xi)^2 + (q/P^*)^2 / \zeta^2 = 1 \quad (4)$$

where ξ and ζ are normalization constants, that define the amplitude of the envelope (Figure 1b).

2.2. Previous Work

In order to gain insights into the relationship between porosity and permeability, and their evolution in response to an applied stress field, numerous experimental studies have been conducted on a variety of rock types over a range of boundary conditions [e.g., David et al., 1994; Zhu and Wong, 1997; Crawford and Yale, 2002; Bernabé et al., 2003; Baud et al., 2012; Kitajima et al., 2012]. These studies have shown that mineralogical composition, initial porosity, grain size and degree of compaction play fundamental roles in the deformation and mode of failure of sediments associated with micromechanical interaction between grains and thus the macroscopic evolution of permeability.

The evolution of permeability during triaxial deformation tests has been investigated for sandstones with initial porosities ranging from 15 to 35% [Zhu and Wong, 1997; Heriland and Raab, 2001; Crawford and Yale, 2002; Bésuelle et al., 2003; Holcomb and Olsson, 2003; Vajdova et al., 2004a,b; Fortin et al., 2005; Tembe et al., 2008; Baud et al., 2012]. Zhu and Wong [1997] documented a direct relationship between permeability and porosity as deviatoric stress was increased, characterized by a monotonic decrease in permeability with increasing strain, independent of whether the sample showed shear localization. Similarly, Vajdova et al. [2004a], conducted triaxial deformation experiments on Bentheim sandstone with an initial porosity of 22%. They found that at lower effective pressures, between 10 MPa and 30 MPa, all samples failed via shear localization and that permeability decreased as strain increased. However, porosity showed a different evolution, from a dilatant behavior at the lowest pressure (10 MPa), to a negligible change in porosity at the highest pressure (30 MPa). Microstructural analysis revealed the formation of compaction bands with intense damage (i.e., reduced pore size and connectivity) and a sharp transition to the surrounding damage zone. In the cataclastic flow regime, they observed a decrease in permeability with porosity reduction. They showed that permeability evolution depends strongly on strain localization, and that the development of localized failure in discrete compaction bands is the cause of the most significant reduction in permeability. Recently, Baud et al. [2012] performed a systematic study on the evolution of permeability associated with shear localization along compaction bands for different sandstones. They found that permeability reduction is controlled by the orientation at which compaction bands propagate and by their connectivity.

Vajdova et al. [2004b] compared limestones and chalk under hydrostatic and triaxial deformation. They studied samples with a range of initial porosities ($3\% < \phi < 26\%$ for limestone, and $38\% < \phi < 45\%$ for chalk) and showed an evolution of mechanical behavior from brittle failure at low confining pressures (10–30 MPa), to a

Table 1. Summary of Experimental Boundary Conditions, Critical Stress States and Permeability

Experiment Number	Applied Stresses (MPa)	Loading Path	Starting Porosity (%)	Yield Stress (MPa)	Permeability	
					k (m ²)	σ _m (MPa)
p3158	P _c = 3–52	Hydrostatic Loading	42.45	39 (P*)	1.63 × 10 ⁻¹⁴	1
	P _p = 2				1.09 × 10 ⁻¹⁴	30
	P _e = 50				7.47 × 10 ⁻¹⁵	50
p3247	P _c = 4.5	Triaxial Loading	44.31	10.3	1.54 × 10 ⁻¹⁴	1
	P _p = 2				1.20 × 10 ⁻¹⁴	2.5
	P _e = 2.5				5.12 × 10 ⁻¹⁵	11.1
p3248	P _c = 7	Triaxial Loading	45.52	14	3.54 × 10 ⁻¹⁴	1
	P _p = 2				2.83 × 10 ⁻¹⁴	5
	P _e = 5				1.95 × 10 ⁻¹⁴	13.8
p3329	P _c = 9	Triaxial Loading	41.46	18.2	1.21 × 10 ⁻¹⁴	1
	P _p = 2				1.06 × 10 ⁻¹⁴	7
	P _e = 7				8.24 × 10 ⁻¹⁵	19
p3157	P _c = 12	Triaxial Loading	43.39	20 (C*)	2.87 × 10 ⁻¹⁴	1
	P _p = 2				2.48 × 10 ⁻¹⁴	10
	P _e = 10				1.57 × 10 ⁻¹⁴	21.2
p3160	P _c = 32	Triaxial Loading	44.02	36 (C*)	3.26 × 10 ⁻¹⁴	1
	P _p = 2				2.00 × 10 ⁻¹⁴	30
	P _e = 30				1.02 × 10 ⁻¹⁴	41.1

“mixed” behavior characterized by shear enhanced compaction followed by dilation for confining stresses up to 50 MPa. They did not report on permeability.

Existing work highlight the broad range of poromechanical processes that occur during both elastic (i.e., brittle shear localization) and inelastic deformation (i.e., ductile cataclastic flow). A primary goal of our study is to extend the range of conditions for which careful laboratory results are available and to explore the relationship between permeability, porosity and the mode of deformation and failure for porous siliciclastic sediments.

3. Experimental Methods

3.1. Sample Characterization and Preparation

The Marcellus Formation is the lowest unit of the Hamilton Group, deposited in a relatively deep, oxygen-deficient marine environment during Middle Devonian time. It is composed of black shale, with subunits of lighter shales and interbedded siltstone. We performed triaxial deformation experiments on samples recovered from an outcrop in the vicinity of Newton Hamilton, PA, USA. Our samples come from interbeds, with a thickness between 30 and 50 cm, within the Marcellus Formation. The interbeds are characterized by isotropic, very light and fine-grained (grain radius ~70 μm) cohesive quartzose siltstone, in contrast to the surrounding fissile shale, with little to no sign of weathering alteration. XRD analyses revealed a mineralogical composition of quartz (80.7%), smectite + illite (14.9%), and pyrite (0.3%).

For our experiments, we cored cylindrical samples 50 mm in length and 25 mm in diameter from a single, large intact block. Cylinders were ground flat and parallel on each end. Specimens were dried for 72 h at T = 50°C, and then saturated, using de-ionized water under vacuum for 48 h prior to experiments. Initial porosity was calculated as:

$$\phi = V_{v0} / V_{T0} \tag{5}$$

where V_{v0} is the volume of voids, calculated by the difference in weight between the dry and saturated sample, and V_{T0} is the initial total volume. The initial porosity of our samples ranged from 41 to 45.5% (Table 1).

3.2. Experimental Apparatus and Procedure

Triaxial deformation experiments were performed using a biaxial loading frame equipped with a true-triaxial pressure vessel (Figure 2) (for details, see Samuelson *et al.* [2009]). Rock samples were loaded axially between by two stainless steel end platens, equipped with internal channels for fluid flow, and subjected to confining pressure applied using a silicone hydraulic oil (XCEL THERM 600 oil, Radco Industries). Samples were jacketed using poly-olefin heat-shrink tubes and sealed using steel wires and rubber O-rings in order to isolate the sample from the confining oil. Pore pressure lines were connected to the steel loading platens of the sample assembly within the pressure vessel (Figure 2). The pressure vessel is equipped with a main access port for the vertical ram, sealed internally by sliding, dynamic seals.

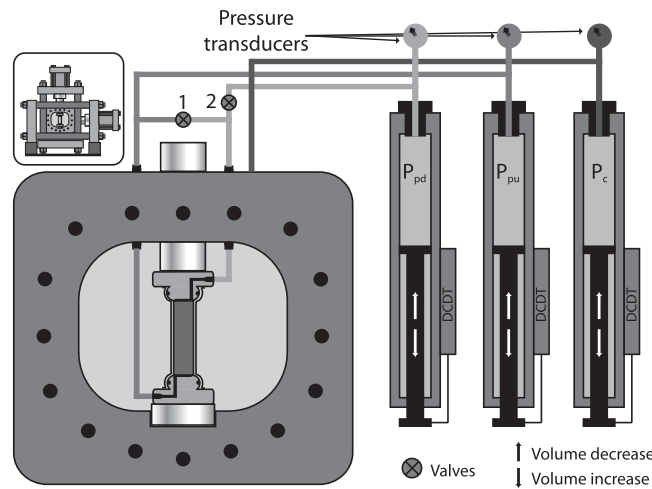


Figure 2. Triaxial pressure vessel and sample assembly. (right) Pressure intensifiers for pore pressure up-stream (P_{pu}), down-stream (P_{pd}), and confining pressure (P_c). Inset shows pressure vessel cell within biaxial load frame.

Upstream pore pressure (P_{pu}), downstream pore pressure (P_{pd}), and confining pressure (P_c) were applied via three separate servo-controlled intensifiers (accuracy of ± 7 kPa), connected to the pressure vessel (Figure 2). A direct current displacement transducer (DCDT), with an accuracy of $\pm 0.1 \mu\text{m}$, was fixed between the vertical piston and the biaxial frame, outside of the vessel. The relative movement of the loading piston with respect to the load frame and pressure vessel is measured by the DCDT and reported as axial displacement at the top of the rock sample, after correcting for the apparatus stiffness, which has a nominal value of $0.35 \text{ kN}/\mu\text{m}$. Vertical load was measured using a strain gauge load cell having an accuracy of $\pm 0.5 \text{ N}$. The pore pressure

system was configured to minimize the total pore volume in the system in order to accurately measure changes in water volume during loading under fully drained boundary conditions, and to measure permeability using the constant head method at different stages of the experiment (Figure 2). Throughout each experiment, we recorded stresses, pressures, displacements and fluid volumes (or flow rates) continuously at 10 kHz using a 24-bit analog to digital system and averaged values for storage at 1–100 Hz depending on the loading rates and conditions.

We used the same loading procedure in all experiments (Figure 3), so that we could assess reproducibility and accurately compare results across our suite of tests (Table 1). In order to remove air within the sample, prior to establishing a pore fluid pressure, we pulled a vacuum on P_{pd} , while P_{pu} was held at a small value, until only water flowed from the pore pressure line. After the specimen was fully saturated, we increased pressure under hydrostatic conditions to an effective pressure of 1 MPa by slowly and simultaneously increasing P_c and P_p to 3 MPa and 2 MPa, respectively, while keeping $P_e < 1 \text{ MPa}$. During this time, leak inspection was performed to ensure that the specimen was completely isolated from the confining medium. Confining pressure was then increased while P_p was kept constant at 2 MPa, through steps of 2.5 MPa every 10 min until we reached the P_e targets of 2.5, 5, 7, 10 and 30 MPa (Table 1, Figure 3). Deviatoric stress was then applied by increasing σ_1 at a constant strain rate of $2 \times 10^{-4} \text{ s}^{-1}$ (axial displacement rate of $0.1 \mu\text{m}/\text{s}$) while maintaining constant confining pressure and pore pressure. At the end of triaxial deformation the vertical ram was stopped, and the sample was unloaded.

Specimens were then carefully removed from the pressure vessel and collected for further investigation.

Throughout all experiments we monitored the evolution of porosity via changes in pore volume within the sample. This was done by controlling the pore fluid pressure intensifiers in load mode servo-feedback and recording changes in piston displacement, to recover changes in water volume delivered to/from the samples. We calculate volumetric strain (ϵ_v) as:

$$\epsilon_v = \Delta V / V_{T0} \quad (6)$$

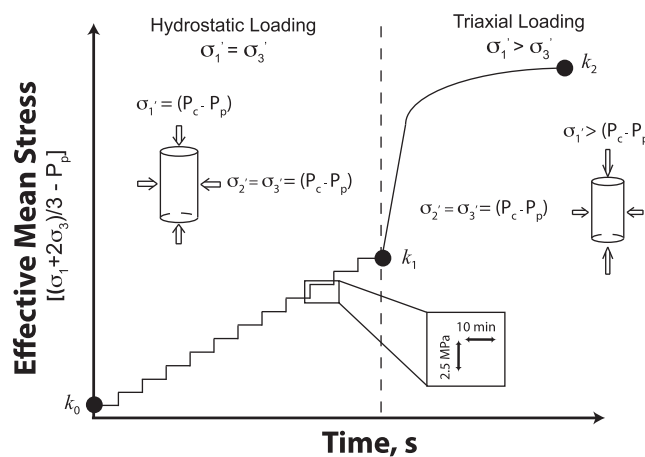


Figure 3. Schematic diagram, illustrating our typical experimental procedure for hydrostatic and triaxial loading. Permeability measurements (k_0 , k_1 , k_2) are taken at different stages of the experiment (solid circles).

where ΔV is the change in sample volume during the experiment and

V_{T0} is the initial total sample volume. Changes in porosity ($\Delta\phi$) during the experiment were then calculated as:

$$\Delta\phi = \phi_0 - \phi = \frac{V_{V0}}{V_{T0}} - \frac{V_V}{V_T} = \frac{V_{V0}}{(V_{V0} + V_S)} - \frac{V_V}{(V_V + V_S)} \quad (7)$$

where V_V is the volume of voids, V_T is the total sample volume and V_S is the volume of the solid, which is assumed to be incompressible. The relationship between volumetric strain (ε_v) and porosity (ϕ) is then expressed as:

$$\phi = \frac{\phi_0 - \varepsilon_v}{100 - \varepsilon_v} * 100 \quad (8)$$

Permeability was measured at three stages during each experiment: (1) at $P_e = 1$ MPa, indicated as k_0 , (2) at the P_e target for each experiment (k_1) prior to triaxial loading, and (3) at the end of triaxial loading (k_2) (Figure 3). For the hydrostatic loading experiment, we measured permeability at P_e of 1, 30 and 50 MPa. We calculated permeability using Darcy's law:

$$k = \frac{Q}{A\eta} \frac{dl}{dp_p} \quad (9)$$

where k is the sample permeability (m^2), Q is the measured flow rate (m^3s^{-1}), A is the cross-sectional area (m^2), η is the viscosity of water (MPa s), ΔP_p is the imposed differential pore pressure (MPa), and dl is the sample length. We assume $\eta = 1.002 \times 10^{-9}$ MPa s, and define dl from the axial displacement and Q as the average value of the flow rates measured at the up-stream (Q_u) and down-stream (Q_d) pumps. To ensure steady state flow conditions, we waited until the flow rate difference, between Q_u and Q_d , was less than 5%.

4. Experimental Results

4.1. Mechanical Data

During hydrostatic loading ($\sigma_1 = \sigma_2 = \sigma_3$), deformation evolves through three distinct stages as defined by the relationship between effective mean stress and volumetric strain (Figure 4). During the first stage, at low effective mean stress ($1 < \sigma'_m < 12$ MPa), the stress-strain curve is nonlinear and concave up, indicative

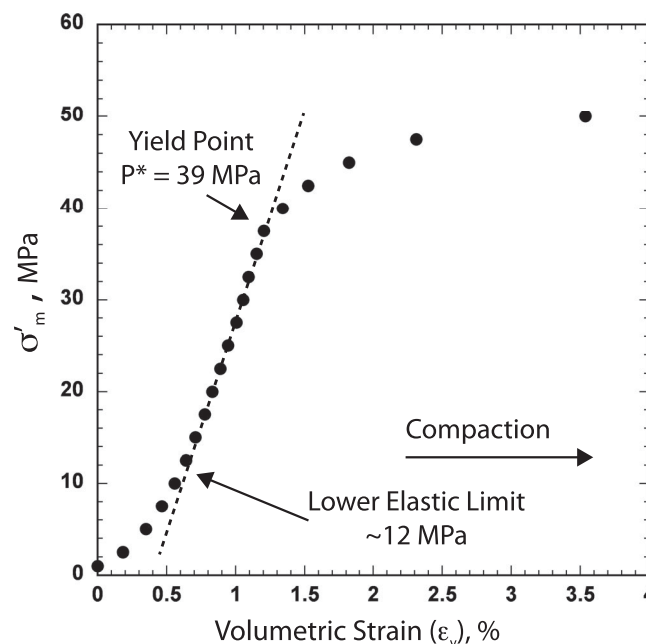


Figure 4. Effective mean stress versus volumetric strain during hydrostatic loading. The sample compacts with increasing load in three distinct stages: (a) inelastic behavior at low applied stress, (b) linear-elastic behavior (indicated by the dashed line), (c) unrecoverable strain beyond the critical stress P^* .

of crack closure with increasing σ'_m (Figure 4). During the second stage, for $\sigma'_m > 12$ MPa, the stress-strain curve is quasi-linear and characterized by linear compressibility of $\beta = 2.1 \times 10^{-8} Pa^{-1}$. The third stage is marked by an inflection in the stress-strain curve and enhanced compaction corresponding to the critical hydrostatic stress when grain crushing begins, P^* . For stresses above P^* , samples compact inelastically and volumetric strain accumulates without appreciable increase in mean effective stress (Figure 4).

Triaxial deformation experiments at applied effective pressures (P_e) from 2.5 to 30 MPa show a range of mechanical responses from brittle to ductile (Figures 5 and 6). During hydrostatic loading, up to the target P_e , in all experiments, except the experiment at $P_e = 7$ MPa, samples compact following the hydrostatic loading path (Figures 5a and 5b). The experiment at $P_e = 7$ MPa shows a positive offset in

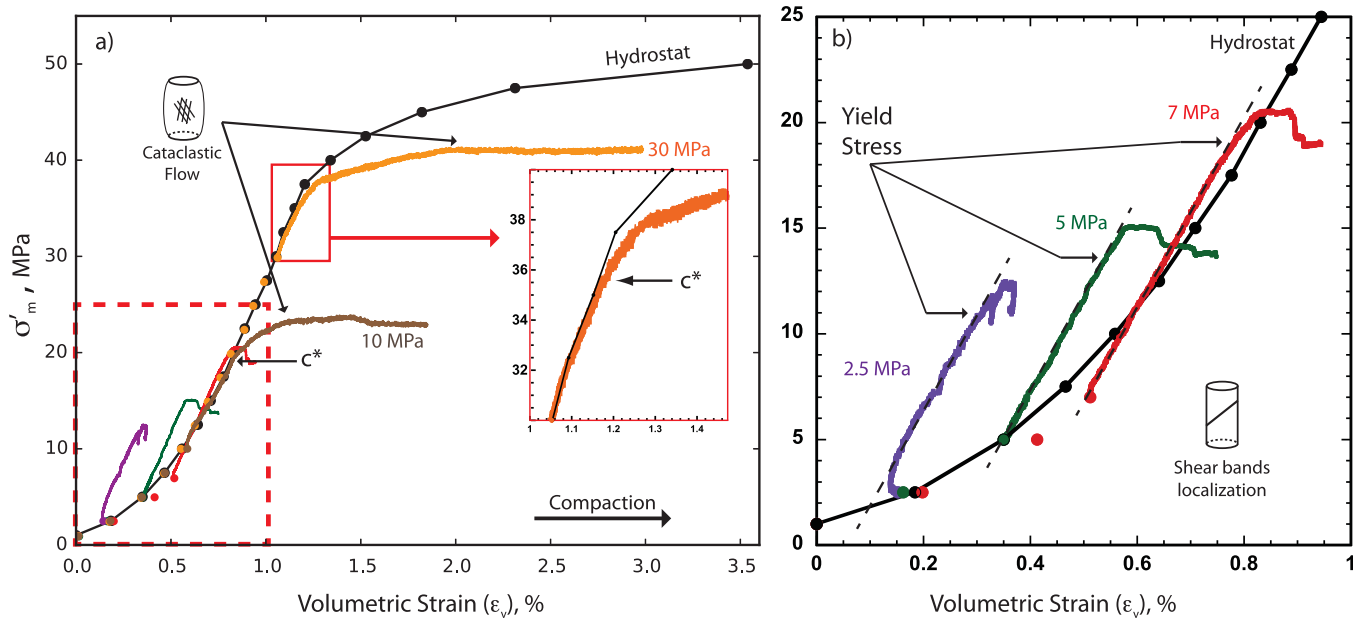


Figure 5. Results from hydrostatic and triaxial loading experiments showing effective mean stress plotted against volumetric strain (compaction is positive). (a) Data for hydrostatic loading experiment (black line) showing P^* at 39 MPa. Full lines represent triaxial loading experiments for each P_e investigated (labeled on the curve). C^* represents the yield point for experiments conducted at $P_e = 10$ and 30 MPa, and marks the onset of shear-enhanced compaction and failure through cataclastic flow. Inset shows details for C^* at $P_e = 30$ MPa. (b) Triaxial loading experiments for $2.5 \text{ MPa} \leq P_e \leq 7 \text{ MPa}$, showing compactive behavior and brittle stress drop. Dashed black lines represent the fit for quasi-linear elastic loading and the deviation from it marks the yield stress.

volumetric strain by 0.1 % at the end of the hydrostatic loading, likely due to the fact that this sample had the lowest initial porosity (Figure 5b and Table 1). Upon the initiation of triaxial loading, where deviatoric stress is applied, all experiments show departures from the hydrostatic loading path. The experiment conducted at

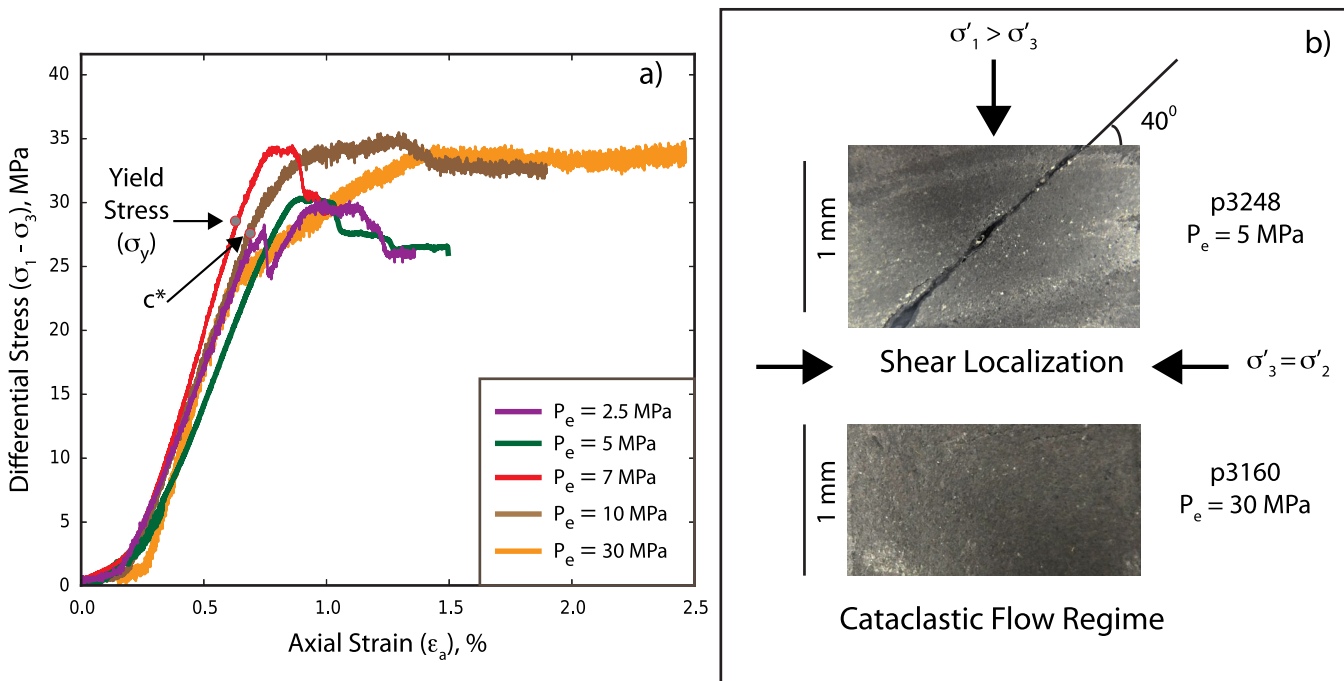


Figure 6. (a) Differential stress as a function of axial strain during triaxial deformation experiments for each effective pressure investigated. We report the critical stress state at yield for the experiments at $P_e = 7$ and 10 MPa with gray circles. (b) Images of postexperiment specimen obtained with high-resolution laser scanner for two samples deformed at different initial effective pressure. The samples are oriented along the σ_1 direction. (top) $P_e = 5 \text{ MPa}$. Deformation is characterized by shear localization along a discrete plane which cuts across the entire sample at an angle of $\sim 40^\circ$ to the direction of σ_1 . (bottom) $P_e = 30 \text{ MPa}$. The sample failed via cataclastic flow and shows pervasive deformation.

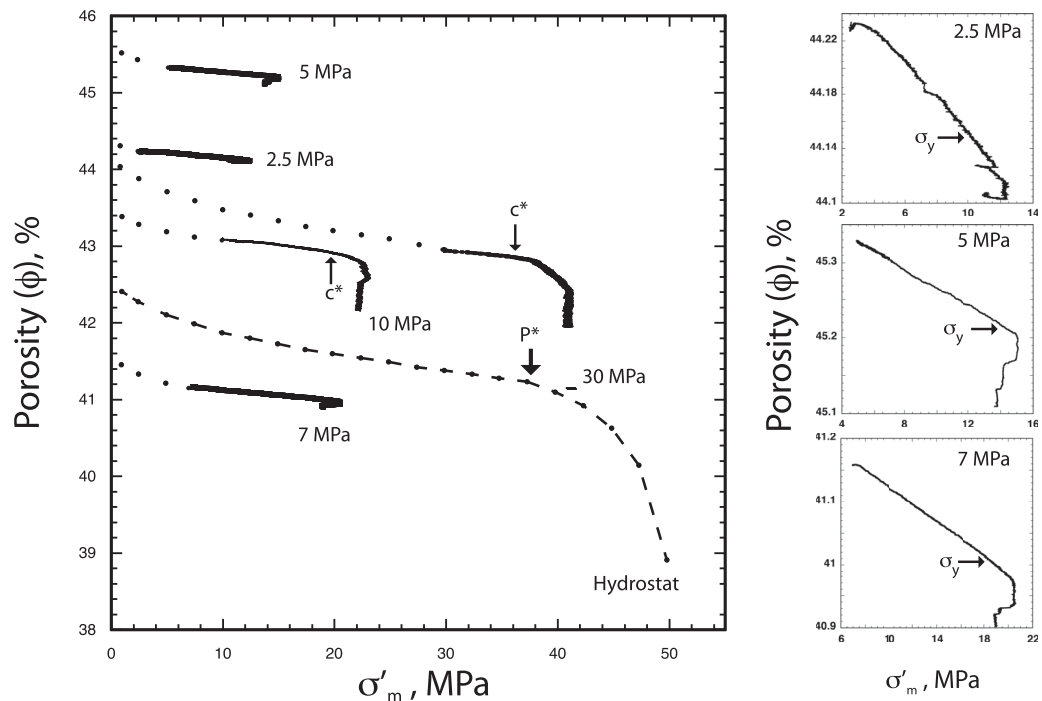


Figure 7. Evolution of porosity as a function of effective mean stress for hydrostatic and triaxial loading experiments. Black, full circles indicate hydrostatic loading, and lines indicate triaxial loading. Data show a constant loss in porosity during hydrostatic loading and the first stage of triaxial loading, followed by an accelerated porosity reduction caused by the applied deviatoric stress. (right) Zoom in portions of experiments at 2.5, 5 and 7 MPa effective pressure.

the lowest confining pressure we tested ($P_e = 2.5$ MPa) shows an initial phase of dilation, followed by quasi-linear compaction. With continued loading, departure from quasi-linear behavior indicates macroscopic sample yielding (σ_y), followed by a stage of compaction and finally a stress drop. Deformation continues until a steady-state residual strength is attained (Figures 5b and 6a). Samples deformed at P_e of 5 and 7 MPa show compaction throughout the deformation path. After the first stage, characterized by quasi-linear stress-strain behavior, an acceleration in compaction marks sample yield, which is then followed by a stress drop (Figure 5b). Postexperiment visual observations show failure by shear localization, with the through-going propagation of shear bands (Figure 6b). For experiments at higher confining pressures ($P_e = 10$ and 30 MPa), samples deform linear-elastically along the hydrostatic loading curve even after triaxial loading is initiated. Deviation from linear-elastic behavior, corresponding with an acceleration in compaction rate, marks sample yielding, and defines the yield stress C^* (Figure 5a). Beyond C^* , shear enhanced compaction dominates and volumetric strain accumulates rapidly with only minor increases in both differential stress and mean stress (Figure 5a). These samples fail by cataclastic flow, which is confirmed by postexperiment visual observation (Figure 6b).

Figure 6a shows a positive relation between sample yielding and P_e in the brittle regime, with the yield stress increasing upon an increase in applied effective pressure. The opposite is true for samples deformed in the ductile regime, with the differential stress at yield point C^* decreasing as P_e is increased from 10 to 30 MPa.

Figure 7 shows the evolution of porosity with mean stress for our range of initial sample porosities, from 41.4 to 45.5%. During hydrostatic loading, independent of initial porosity, we observe similar compaction rates for all experiments. In response to an applied deviatoric stress, we find compaction for all of the P_e investigated during all stages of deformation, with the exception of the experiment at $P_e = 2.5$ MPa which shows some dilation at the beginning of the loading path followed by compaction. Samples that failed through shear localization in discrete shear bands do not show any significant reduction in porosity associated with failure.

4.2. Permeability

We report permeability (k) evolution as a function of effective mean stress for hydrostatic and triaxial deformation experiments (Figure 8 and Table 1). Our data show a clear correlation between sample failure mode

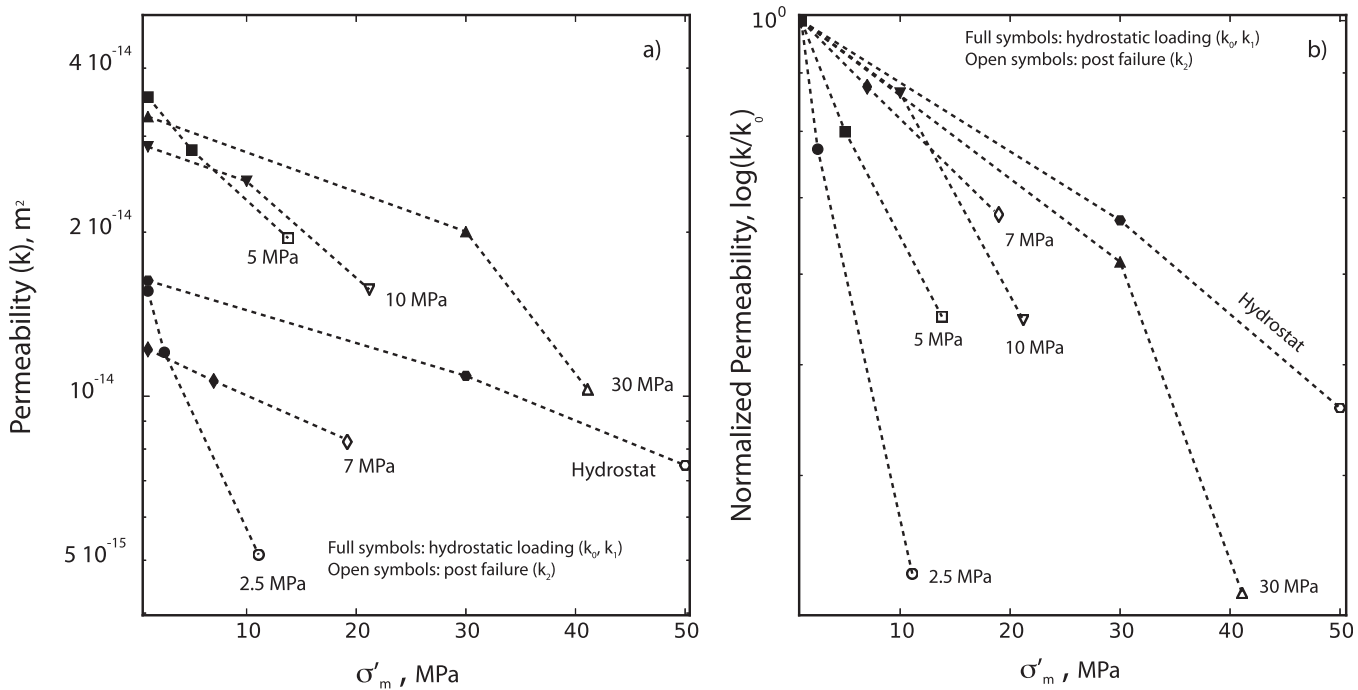


Figure 8. Permeability evolution as a function of effective mean stress during hydrostatic (solid symbols) and triaxial loading (open symbols) for all the experiments. (a) Raw data. Permeability evolves as a function of applied effective pressure and failure mode. (b) Normalized permeability for comparison.

and permeability evolution. Permeability decreases continually with increasing load during hydrostatic loading, accordingly with sample porosity reduction (Figure 7 and Table 1). The values of initial permeability (k_0) at 1 MPa show a small variability that reflects the variability in the values of initial porosity, with values between 1.21×10^{-14} and 3.54×10^{-14} m² (Figure 8a).

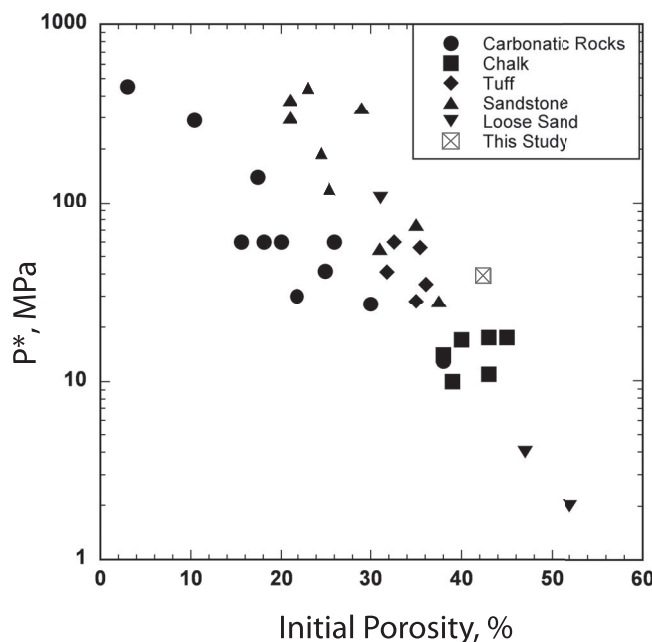


Figure 9. Critical effective pressure (P^*) for the onset of grain crushing under hydrostatic loading as a function of initial porosity for different sedimentary and volcanic rocks. Data are compiled from Tembe et al. [2008], Vajdova et al. [2004a, 2004b], Zhu et al. [2011], Wong et al. [1997], and references therein.

Under triaxial deformation, we observe a different evolution of permeability that depends on the effective confining pressure and the mode of sample failure. At effective pressures of 2.5, 5, and 7 MPa, specimens characterized by shear localization show a quasi-linear decrease in permeability with loading (Figure 8). In the cataclastic flow failure regime, at effective pressures of 10 and 30 MPa, permeability decreases more dramatically in the postyield region (Figure 8, open symbols).

In order to compare permeability data, we normalized our measured permeability by the initial permeability k_0 for each sample (Figure 8b). Figure 8b shows that when failure localizes along discrete shear bands, for experiments at P_e of 2.5, 5 and 7 MPa, permeability assumes a negative correlation with P_e ; the decrease in permeability after shear localization is largest at low initial effective pressures. Conversely, in the ductile

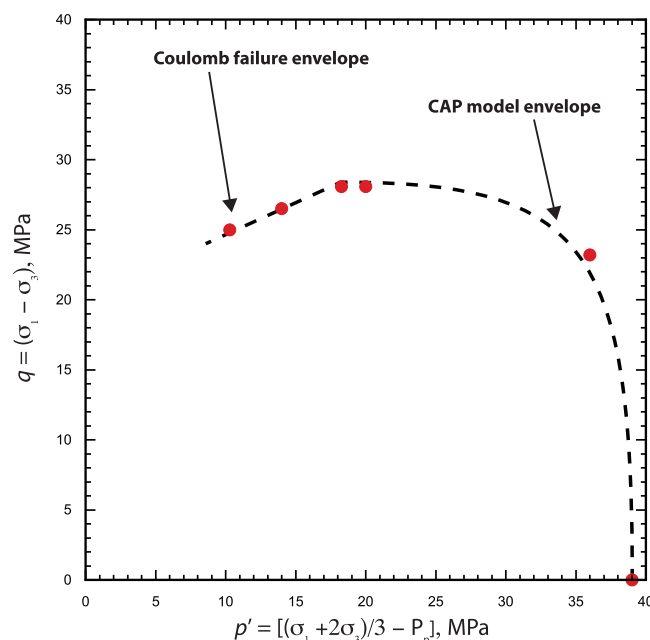


Figure 10. Critical stress state at yield (onset of shear localization) and C^* (onset of shear-enhanced compaction) are shown in q - p' space where q is the differential stress and p' is the effective means stress. Samples that failed via shear localization are characterized by a linear envelope described by a Coulomb-Mohr type failure criteria. Yield points at the onset of shear-enhanced compaction (C^*) describe an elliptical envelope (CAP model) with negative slope.

field, we document that as effective pressure is increased from 10 to 30 MPa permeability decreases accordingly.

5. Discussion

Previous studies have characterized mechanical properties of sandstones with a range of initial porosity values under both hydrostatic and triaxial applied stress fields [Zhu and Wong, 1997; Heriland and Raab, 2001; Crawford and Yale, 2002; Bésuelle et al., 2003; Holcomb and Olsson, 2003; Vajdova et al., 2004a,b; Fortin et al., 2005; Tembe et al., 2008; Baud et al., 2012]. These works have investigated the control of stress state and failure mode on porosity and permeability. Understanding the micro-mechanical processes leading to the brittle-ductile transition in porous sedimentary rocks is of fundamental importance in order to extrapolate laboratory based observations to natural environments (i.e., sedimentary basins, accretionary prisms), where complex stress states have been observed.

Our data show that stress state and deformation mode correlate with the evolution of porosity and permeability. These results indicate that the mode of failure will likely play a fundamental role in controlling fluid distribution and pressure during the burial history of sediments, potentially leading to overpressures or compartmentalization of fluids. In the following, we discuss our experimental results and compare them with previous work, focusing on the relationships between stress state, macroscopic yielding, and associated failure mode in order to understand their impact on porosity and permeability.

5.1. Macroscopic Yielding Under Hydrostatic Loading

We document three main stages of deformation under hydrostatic loading (Figure 4). In Stage 1, at low σ'_m , the stress-strain relation is nonlinear, consistent with crack closure and grain matrix rearrangement through grain sliding and rolling [Karner et al., 2003]. Stage 2 is characterized by quasi-linear stress-strain behavior at intermediate stress, and is followed by Stage 3 and an acceleration in compaction that corresponds to P^* . Above P^* , samples fail by cataclastic flow and pore collapse, which causes irrecoverable strain and permanent deformation [Zhang et al., 1990a; Menéndez et al., 1996].

We summarize the relationship between P^* and initial porosity for a variety of sedimentary and volcanic rocks in Figure 9. We find a log-linear relationship, where P^* decreases as porosity increases, as proposed by Zhang et al. [1990b] based on a Hertzian fracture model. However, we find that mineralogy can appreciably influence the grain crushing pressure, consistent with the theoretical model proposed by Zhu et al. [2007] and experimental results of Tembe et al. [2008]. Comparing P^* between our study and other rock types with similar porosity, such as chalk, we show that our siltstone (with >80% quartz) is characterized by higher P^* than chalk. Tembe et al. [2008] documented an increase of two orders of magnitude in P^* with increasing quartz content in sandstones with similar initial porosity. These observations lead us to hypothesize that mineralogy also plays an important role in the micromechanical processes that drive mechanical compaction under an applied isotropic stress field.

5.2. Critical Failure Envelope

Typically, under both hydrostatic and triaxial deformation, any departure from quasi-linear elastic behavior is taken as sample yielding, and used to determine the macroscopic failure envelope for the material

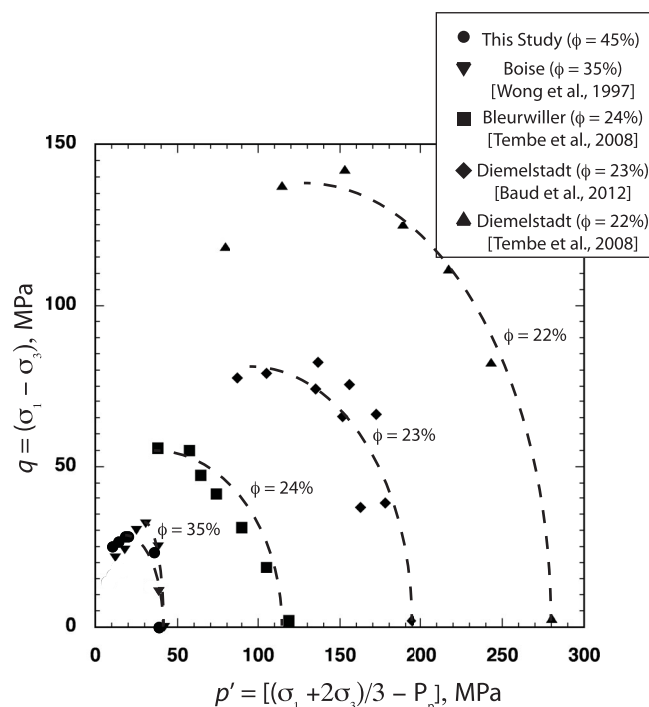


Figure 11. Strength envelope in q - p' space for samples where propagation of shear and compaction bands were observed in laboratory deformation experiments. We report data from this study (circles). We also show data from *Tembe et al.* [2008] on Diemelstadt sandstone (triangles), characterized by an initial porosity of 22% and grain radius $r = 160 \mu\text{m}$, and Bleurwiller (squares) characterized by an initial porosity of 24% and grain radius $r = 224 \mu\text{m}$, *Baud et al.* [2012] on Diemelstadt sandstone (diamonds), characterized by an initial porosity of 23%, and *Wong et al.* [1997] on Boise sandstone (inverted triangles), characterized by an initial porosity of 35% and grain radius $r = 280 \mu\text{m}$.

Our data can be fit by a Coulomb-type failure envelope of the form, $q = 21.02 + 0.7 p'$, at low effective pressures (Figure 10). Combining equations (2) and (3), we report a value for internal friction of $\tan\theta = 0.3$, and an angle of internal friction of $\theta = 20^\circ$. With increasing effective pressure, the evolution of yield strength at the onset of shear-enhanced compaction C^* is characterized by an elliptical cap, as widely observed for sedimentary rocks [i.e., *Wong et al.*, 1997; *Vajdova et al.*, 2004a, 2004b; *Zhu et al.*, 2011; *Baud et al.*, 2012]. We fit the envelope of critical stress states C^* using equation (4) with values of $\zeta = 0.45$ and $\xi = 0.55$ to fit our experimental data [*Di Maggio and Sandler*, 1971]. These values are in agreement with typical values for sandstones (in the range of $\zeta = 0.5$ and $\xi = 0.5$ - 0.7) [*Wong et al.*, 1997]. A comparison between the Marcellus siltstone and different sandstones, with initial porosity values ranging between 22 and 35%, shows self-similar evolution of the yield CAPs (Figure 11). The yield surface expands as porosity decreases, as the compactive yield stress C^* increases with decreasing porosity.

Our data represent weaker materials with lower yield stresses relative to previous work on siliciclastic sediments with lower porosities and larger grain sizes [e.g., *Zhang et al.*, 1990a; *Wong et al.*, 1997; *Vajdova et al.*, 2004b; *Tembe et al.*, 2008; *Baud et al.*, 2012] (Figure 11). These observations confirm that porosity and grain radius exert a strong control on the strength of porous sedimentary rocks. An increase in porosity associated with a smaller grain size lowers the critical stress state for the onset of shear-enhanced compaction.

Postexperiment observations reported for Diemelstadt and Bentheim sandstones under brittle conditions, revealed that shear localizes along discrete shear bands at an angle between 25° and 45° to the σ_1 direction [*Vajdova et al.*, 2004b; *Tembe et al.*, 2008]. We find that for samples deformed at P_e between 2.5 and 7 MPa, shear also localizes along discrete bands at an angle of $\sim 40^\circ$ with σ_1 (Figure 6b). We propose that in siliciclastic sedimentary rocks, porosity has a strong control on the strength, and as a consequence on the brittle-ductile transition, of specimens when a deviatoric stress is applied. However, the deformation style,

following a constitutive yield criteria [e.g., *Karig*, 1990; *Zhang et al.*, 1990b; *Wong et al.*, 1997; *Baud et al.*, 2000; *Crawford and Yale*, 2002; *Kitajima et al.*, 2012; *Rutter and Glover*, 2012]. We follow this approach for the analysis of our experiments, combining a Coulomb-Mohr failure criterion and CAP model.

When we deformed samples under an applied triaxial stress field, we documented an evolution from brittle behavior, characterized by localization of shear, to a cataclastic flow regime, with increasing effective pressure. For lower effective pressures, from 2.5 to 7 MPa, sample yield stress show a positive correlation with increasing P_e , typical of Coulomb-Mohr brittle failure criteria (Figure 6a). For $P_e > 7$ MPa, samples fail via cataclastic flow due to shear-enhanced compaction. In this regime, the yield stress C^* shows a negative relationship with effective pressure, as higher effective pressures result in lower C^* values [*Wong et al.*, 1997] (Figure 5a).

Yield stresses can be analyzed in terms of both the differential stress, q , and effective mean stress, p' (Figure 10).

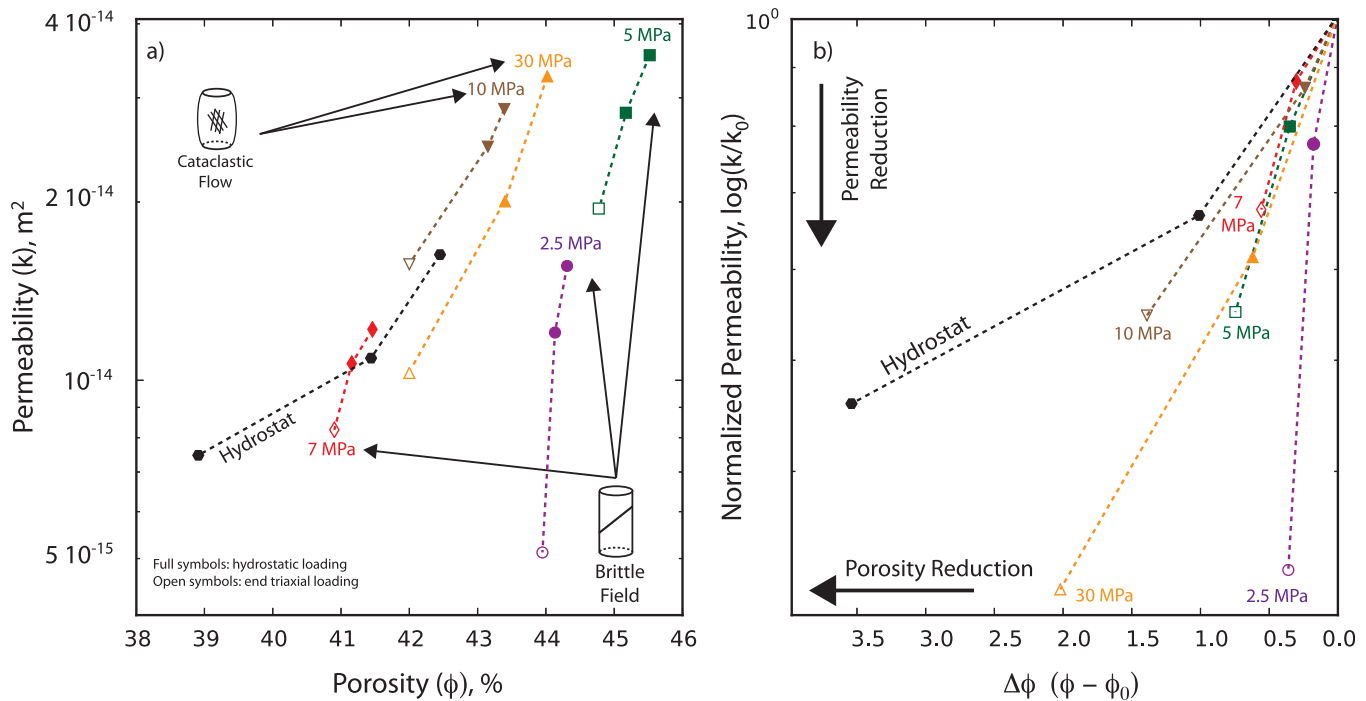


Figure 12. Permeability-porosity relationship for (a) raw data, (b) linear change in porosity porosity and normalized permeability. Full symbols represent permeability measured during hydrostatic loading (k_0 and k_1). Open symbols represent measurements performed at the end of triaxial deformation (k_2).

the angle at which shear localizes in the brittle failure regime, and critical stress state pressure dependence, seems to be a common feature between different siliciclastic rocks, independent of porosity.

5.3. Evolution of Permeability: Shear Localization Versus Cataclastic Flow

Samples deformed at effective pressures between 2.5 and 7 MPa failed through shear localization along discrete planes cross-cutting the specimens (Figure 6). In all three experiments, permeability rapidly decreases after shear localization, but is accompanied by little compaction (i.e., porosity reduction) (Figure 12a), showing a systematic decrease in $\log(k_2/k_1)/(\phi_2 - \phi_1)$ as effective pressure is increased (Figure 12b). In contrast, *Zhu and Wong* [1997] observed a negative relationship between porosity and permeability when shear localized in sandstones with initial porosities ranging from 13 to 35%. At a yield stress state C' , the onset of dilation, brittle failure causes porosity to increase and permeability to decrease. The studies of *Heiland and Raab* [2001] and *Vajdova et al.* [2004a] documented a transition between dilatant brittle failure, at low effective pressures, and compactive shear localization, with increasing effective pressure, as a “mixed mode” of failure in porous sandstones. Their results showed that in the dilatant brittle regime, permeability is negatively correlated with porosity as expected from *Zhu and Wong* [1997]. However, in agreement with our data, in the “mixed mode” regime they documented a decrease in permeability with negligible decrease in porosity associated with shear band localization. Postexperiment observations, in both cases, show that deformation is highly localized in discrete planes developed throughout the sample, characterized by grain comminution, without changes in the porosity of material outside of the shear bands. Conversely, at higher effective pressure, in the cataclastic flow failure regime, we document a positive relationship between permeability and porosity. Above C^* , mechanical compaction causes pore space to decrease and tortuosity to increase, resulting in a decrease in permeability. These observations agree with previous data on sandstones [e.g., *Zhu and Wong*, 1997; *Baud et al.*, 2000].

Our observations indicate that in the brittle failure regime, the propagation of discrete shear bands can act as barriers to fluid flow due to shear localization and grain comminution. This can have important implications for the hydrological properties and fluid distribution at shallow depths (i.e., low effective pressures) within actively deforming systems. In accretionary prisms, fluid pressurization and fluid flow can play a fundamental role in the mechanical response of sediments to an applied stress field [i.e., *Kitajima et al.*, 2012]. The potential generation of fluid overpressures, across shear zones, can act as a weakening mechanism,

lowering the effective pressure acting on the shear planes and favoring the nucleation and/or propagation of seismic rupture. Furthermore, reservoir systems, usually located in sedimentary basins, are areas marked by continuous changes in the stress state with rocks following complex stress and deformation paths due to depletion and/or injection of fluids. For the purposes of oil and gas extraction, the relation between porosity and permeability has important implications for the efficiency of the extraction well. Here we have shown that for high porosity siliciclastic rocks, which likely represent a source for extraction, the relationship between porosity and permeability is largely controlled by the applied stress field and deformation path. In this context, extraction procedures, such as hydraulic fracturing and water flooding, can lower the effective stress, activating brittle deformation associated with microseismicity and permeability barriers within the basin, controlling fluids compartmentalization.

6. Summary

To investigate the coupling between permeability, porosity and mechanical behavior across the brittle ductile transition in porous siltstone ($41.4\% < \phi < 45.5\%$), we performed hydrostatic and triaxial loading experiments over a range of effective pressures, from 2.5 to 50 MPa. Porosity was continuously measured during progressive deformation and permeability was measured at three different characteristic stages of deformation for each experiment. Our hydrostatic loading experiment results in P^* at 39 MPa, as the characteristic pressure for the onset of grain crushing and pore collapse. Triaxial deformation experiments show two different deformation styles as a function of initial applied effective pressure: (1) shear localization in bands, cross-cutting the sample, at effective pressures less than 7 MPa; and (2) failure through cataclastic flow, at effective pressures of greater than 10 MPa.

Comparing our results with previous studies on sedimentary and volcanic rocks of different porosity, we find that mineralogical composition exerts a strong control on P^* . The yield stresses during triaxial deformation are best described by a Coulomb-type failure criteria at low effective pressure, and a CAP model at higher effective pressure. The yield envelope for the Marcellus siltstone with $\sim 44\%$ porosity represents a low-strength end-member when compared with siliciclastic rocks of lower initial porosity.

In both the brittle and ductile regimes, porosity and permeability decrease with increasing strain. When shear localizes, we document an abrupt decrease in permeability associated with intense compaction. This is in contrast with previous studies on siliciclastic rocks with lower porosity, where brittle deformation is usually associated with dilation and an increase in permeability. With increasing effective pressure and strain, permeability and porosity decreases more gradually. Postexperiment observations show that shear localizes along discrete zones, at low effective pressures, without any significant changes in the surrounding bulk porosity. On the other hand, with increasing effective pressure we document pervasive deformation, accordingly with the porosity-permeability relationship observed. Our results imply that permeability is dependent on the deformation style and strain localization. At low effective pressures (i.e., shallow depth), shear localization along discrete bands can act as a barrier to fluid flow, modifying the hydrological properties and distribution of fluids.

Acknowledgments

We thank M. Takahashi and an anonymous reviewer for their constructive comments that helped to improve the quality of this manuscript. This work was supported by NSF grants OCE-0648331, EAR-0746192, and EAR-0950517 to CM and DS. We thank D. Elsworth for his helpful scientific discussion and S. Swavelly for the technical support. Our data are available by FTP transfer by contacting the corresponding author.

References

- Baud, P., A. Schubnel, and T. Wong (2000), Dilatancy, compaction and failure mode in solnhofen limestone, *J. Geophys. Res.*, *105*, 289–303.
- Baud, P., P. Meredith, and E. Townend (2012), Permeability evolution during triaxial compaction of an anisotropic porous sandstone, *J. Geophys. Res.*, *117*, B05203, doi:10.1029/2012JB009176.
- Bernabé, Y., U. Mok, and B. Evans (2003), Permeability-porosity relationships in rocks subjected to various evolution processes, *Pure Appl. Geophys.*, *160*, 937–960.
- Bésuelle, P., P. Baud, and T. Wong (2003), Failure mode and spatial distribution of damage in Rothbach sandstone in the brittle-ductile transition, *Pure Appl. Geophys.*, *160*(5), 851–868, doi:10.1007/PL00012569.
- Bolton, M. (1979), *A Guide to Soil Mechanics*, John Wiley, N. Y.
- Brace, W. F. (1978), Volume changes during fracture and frictional sliding: A review, *Pure Appl. Geophys.*, *116*(4–5), 603–614, doi:10.1007/BF00876527.
- Brantut, N., P. Baud, M. J. Heap, and P. G. Meredith (2012), Micromechanics of brittle creep in rocks, *J. Geophys. Res.*, *117*, B08412, doi:10.1029/2012JB009299.
- Byerlee, J. (1993), Model for episodic flow of high-pressure water in fault zones before earthquakes, *Geology*, *21*, 303–306.
- Byrne, D., D. Davis, and L. Sykes (1988), Loci and maximum size of thrust earthquakes and the mechanics of the shallow region of subduction zones, *Tectonics*, *7*(4), 833–857.

- Crawford, B. R., and D. P. Yale (2002), Constitutive modeling of deformation and permeability: Relationships between critical state and micromechanics, paper presented at SPE/ISRM Rock Mechanics Conference, pp. 1–10, Soc. of Pet. Eng., Richardson, Tex., doi:10.2118/78189-MS.
- Curran, J. H., and M. M. Carroll (1979), Shear stress enhancement of void compaction, *J. Geophys. Res.*, *84*, 1105–1112, doi:10.1029/JB084iB03p01105.
- David, C., T. F. Wong, W. Zhu, and J. Zhang (1994), Laboratory measurement of compaction-induced permeability change in porous rocks: Implications for the generation and maintenance of pore pressure excess in the crust, *Pure and Applied Geophysics*, *PAGEOPH*, *143*, 425–456, doi:10.1007/BF00874337.
- Di Maggio, F. L., and I. S. Sandler (1971), Material model for granular soils, *J. Eng. Mech. Div.*, *97*(3), 935–950.
- Drucker, D. C., W. Prager, and H. T. Greenberg (1952), Extended limit design theorems for continuous media, *Q. Appl. Math.*, *9*(4), 381–389.
- Ellsworth, W. L. (2013), Injection-induced earthquakes, *Science*, *341*(2), doi:10.1126/science.1225942.
- Fortin, J., A. Schubnel, and Y. Guéguen (2005), Elastic wave velocities and permeability evolution during compaction of Bleurswiller sandstone, *Int. J. Rock Mech. Min. Sci.*, *42*(7–8), 873–889, doi:10.1016/j.ijrmms.2005.05.002.
- Fossen, H., R. A. Schultz, Z. K. Shipton, and K. Mair (2007), Deformation bands in sandstone: A review, (Davis 1999), vol. 164, pp. 755–769, doi:10.1144/0016-76492006-036.
- Heiland, J., and S. Raab (2001), Experimental investigation of the influence of differential stress on permeability of a Lower Permian (Rotliegend) sandstone deformed in the brittle deformation, *Phys. Chem. Earth*, *26*(1), 33–38.
- Holcomb, D. J., and W. A. Olsson (2003), Compaction localization and fluid flow, *J. Geophys. Res.*, *108*(B6), 2290, doi:10.1029/2001JB000813.
- Hubbert, M., and W. Rubey (1959), Role of fluid pressure in mechanics of overthrust faulting, *Geol. Soc. Am.*, *70*, 115–166.
- Hyndman, R., and K. Wang (1995), The rupture zone of Cascadia great earthquakes from current deformation and the thermal regime, *J. Geophys. Res.*, *100*, 22,133–22,154.
- Hyndman, R. D., K. Wang, G. D. Spence, and T. Yuan (1993), Tectonic sediment thickening, fluid expulsion, and the thermal regime of subduction zone accretionary prisms: The Cascadia Margin off Vancouver Island, *J. Geophys. Res.*, *98*, 21,865–21,876.
- Improta, L., L. Valoroso, D. Piccinini, and C. Chiarabba (2015), A detailed analysis of wastewater-induced seismicity in the Val d'Agri oil field (Italy), *Geophys. Res. Lett.*, *42*, 2682–2690, doi:10.1002/2015GL063369.
- Kaproth, B. M., S. M. Cashman, and C. Marone (2010), Deformation band formation and strength evolution in unlithified sand: The role of grain breakage, *J. Geophys. Res.*, *115*, B12103, doi:10.1029/2010JB007406.
- Karig, D. E. (1990), Experimental and observational constraints on the mechanical behaviour in the toes of accretionary prisms, *Geol. Soc. Spec. Publ.*, *54*(1), 383–398, doi:10.1144/GSL.SP.1990.054.01.35.
- Karner, S. L., F. M. Chester, A. K. Kronenberg, and J. S. Chester (2003), Subcritical compaction and yielding of granular quartz sand, *Tectonophysics*, *377*(3–4), 357–381, doi:10.1016/j.tecto.2003.10.006.
- Karner, S. L., J. S. Chester, F. M. Chester, A. K. Kronenberg, and A. Hajash (2005), Laboratory deformation of granular quartz sand: Implications for the burial of clastic rocks, *AAPG Bull.*, *89*(5), 603–625, doi:10.1306/12200404010.
- Kitajima, H., F. M. Chester, and G. Biscontin (2012), Mechanical and hydraulic properties of Nankai accretionary prism sediments: Effect of stress path, *Geochem. Geophys. Geosyst.*, *13*, Q0AD27, doi:10.1029/2012GC004124.
- Magee, M. and M. Zoback (1993), Evidence for a weak interplate thrust fault along the northern Japan subduction zone and implications for the mechanics of thrust faulting and fluid expulsion, *Geology*, *21*, 809–812.
- Marone, C., and C. Scholz (1988), The depth of seismic faulting and the upper transition from stable to unstable slip regimes, *Geophys. Res. Lett.*, *15*, 621–624.
- Menéndez, B., W. Zhu, and T. Wong (1996), Micromechanics of brittle faulting and cataclastic flow in Berea sandstone, *J. Struct. Geol.*, *18*(1), 1–16.
- Moore, J. and Vrolijk, P. (1992), Fluids in accretionary prisms, *Rev. Geophys.*, *30*, 113–135.
- Roscoe, K. H., A. N. Schofield, and C. P. Wroth (1958), On the yielding of soils, *Géotechnique*, *8*(1), 22–53.
- Rutter, E. H., and C. T. Glover (2012), The deformation of porous sandstones: are Byerlee friction and the critical state line equivalent?, *J. Struct. Geol.*, *44*, 129–140, doi:10.1016/j.jsg.2012.08.014.
- Samuelson, J., D. Elsworth, and C. Marone (2009), Shear-induced dilatancy of fluid-saturated faults: Experiment and theory, *J. Geophys. Res.*, *114*, B12404, doi:10.1029/2008JB006273.
- Sibson, R. (1982), Fault zone models, heat flow, and the depth distribution of earthquakes in the continental crust of the United States, *Bull. Seismol. Soc. Am.*, *72*(1), 151–163.
- Tembe, S., P. Baud, and T. Wong (2008), Stress conditions for the propagation of discrete compaction bands in porous sandstone, *J. Geophys. Res.*, *113*, B09409, doi:10.1029/2007JB005439.
- Vajdova, V., P. Baud, and T. Wong (2004a), Compaction, dilatancy, and failure in porous carbonate rocks, *J. Geophys. Res.*, *109*, B05204, doi:10.1029/2003JB002508.
- Vajdova, V., P. Baud, and T. Wong (2004b), Permeability evolution during localized deformation in Bentheim sandstone, *J. Geophys. Res.*, *109*, B10406, doi:10.1029/2003JB002942.
- Vrolijk, P. (1990), On the mechanical role of smectite in subduction zones, *Geology*, *18*, 703–707.
- Wong, T., C. David, and W. Zhu (1997), The transition from brittle faulting to cataclastic flow in porous sandstones: Mechanical deformation, *J. Geophys. Res.*, *102*, 3009–3025, doi:10.1029/96JB03281.
- Zhang, J., T. Wong, T. Yanagidani, and D. Davis (1990a), Pressure induced microcracking and grain crushing in Berea and Boise sandstones: Acoustic emission and quantitative microscopy measurements, *Mech. Mater.*, *9*, 1–15.
- Zhang, J., T.-F. Wong, and D. M. Davis (1990b), Micromechanics of pressure-induced grain crushing in porous rocks, *J. Geophys. Res.*, *95*, 341–352, doi:10.1029/JB095iB01p00341.
- Zhu, W., and T. Wong (1997), The transition from brittle faulting to cataclastic flow: permeability evolution, *J. Geophys. Res.*, *102*, 3027–3041.
- Zhu, W., L. G. J. Montési, and T. F. Wong (2007), A probabilistic damage model of stress-induced permeability anisotropy during cataclastic flow, *J. Geophys. Res.*, *112*, B10207, doi:10.1029/2006JB004456.
- Zhu, W., P. Baud, S. Vinciguerra, and T. Wong (2011), Micromechanics of brittle faulting and cataclastic flow in Alban Hills tuff, *J. Geophys. Res.*, *116*, B06209, doi:10.1029/2010JB008046.
- Zoback, M. (2012), Managing the seismic risk posed by wastewater disposal, *Earth*, 38–43.